Solar Energy Materials & Solar Cells 253 (2023) 112210

Contents lists available at ScienceDirect

Solar Energy Materials and Solar Cells

journal homepage: www.elsevier.com/locate/solmat

Design and analysis of Sb_2S_3/Si thin film tandem solar cell

M. Okil [a], Ahmed Shaker [b,*], Ibrahim S. Ahmed [a], Tarek M. Abdolkader [a], Marwa S. Salem [c,d]

[a] Department of Basic Engineering Sciences, Benha Faculty of Engineering, Benha University, Benha, Egypt
[b] Department of Engineering Physics and Mathematics, Faculty of Engineering, Ain Shams University, Cairo, Egypt
[c] Department of Computer Engineering, College of Computer Science and Engineering, University of Ha'il, Ha'il, Saudi Arabia
[d] Department of Electrical Communication and Electronics Systems Engineering, Faculty of Engineering, Modern Science and Arts University (MSA), Cairo, Egypt

ARTICLE INFO

Keywords:
Thin film tandem
Sb_2S_3
Thin film c-Si
HTL-Free
CBO
Current matching
TCAD simulation
Power conversion efficiency

ABSTRACT

Antimony sulfide (Sb_2S_3) and thin crystalline silicon (c-Si) are considered suitable top- and bottom-cell candidates for tandem solar cells (TSCs), owing to their natural abundance, non-toxicity, cost-competitiveness, and complementary bandgaps. The current work proposes and investigates a two-terminal (2T) monolithic Sb_2S_3/Si thin film TSC via TCAD simulation. The Sb_2S_3 cell, with a bandgap of 1.7 eV, is utilized as a top sub-cell, and the bottom sub-cell is utilized by a thin c-Si cell having a bandgap of 1.12 eV. The calibrated standalone top and bottom cells provide a power conversion efficiency (η) of 4.31% and 14.26%, respectively. Upon incorporating the two cells into a 2T Sb_2S_3/Si monolithic TSC, the resultant tandem cell achieves an η of 10.10% implying that the top cell should be optimized in order to get a tandem efficiency higher than the bottom cell. Thus, the Sb_2S_3 cell is optimized by designing the cell without the organic hole transport layer (HTL) (resulting in an np heterojunction) and engineering the conduction band offset (CBO) between the electron transport layer (ETL) and the Sb_2S_3 absorber. Then, the tandem structure is optimized starting from the ETL thickness and doping concentration. Also, the impact of changing the absorber defect density and the series resistance of the top cell on the TSC performance is investigated to demonstrate the maximum available η. At reduced defect density and series resistance, the overall efficiency of the tandem cell is improved to 19.51%. Furthermore, we explored the impact of top and bottom absorber thicknesses on TSC working metrics. At the designed matching point, the tandem efficiency is enhanced to 23.25%, and J_{sc} also boosts to 17.24 mA/cm^2. The simulation study is intended to provide a tandem configuration that is based on an all-thin-film design which may be suitable for applications like wearable electronics due to its flexibility. All TCAD simulations are performed using the Silvaco Atlas simulator under standard one Sun (AM1.5G, 1000 W/m^2) illumination.

1. Introduction

One of the technical solutions for reducing the cost of photovoltaic (PV) power generation is to increase solar cell efficiency by designing tandem solar cells with several absorption layers and complementary bandgaps [1–4]. Schematically, tandem devices can be designed in either 2T, 4T, or 3T configurations. The 2T tandem configuration combines wide and narrow bandgap p-n junctions which serve as the top and bottom cells, respectively. The two sub-cells are electrically connected via an interlayer known as the recombination layer or tunneling junction. However, although the two cells of the 4T tandem device are internally separated, they are coupled to combine their full output power [5]. E. Warren et al. [6] recently presented a hybrid tandem photovoltaics configuration known as a 3T tandem configuration. Despite its simplicity of fabrication, external wiring on the front and rear of the solar cell stack is required. For cost-effective applications, the 2T arrangement is preferred due to its reduced fabrication steps. Yet, the top cell of the 2T device is manufactured atop the bottom, making the synthesis process more challenging [7]. Moreover, selecting the top and bottom sub-cells concerning their bandgaps is critical to the performance of both 2T and 4T architectures. The theoretical analyses that have been published offer a guided direction for the choice of optimal bandgap sub-cells. In this context, a 2T monolithic tandem configuration with 1.7 eV top and 1.12 eV bottom cells can accomplish a high conversion efficiency of up to 40% [8].

In addition, tandem cells have been utilized commercially for a wide range of absorbers, from relatively inexpensive hydrogenated amorphous silicon (a-Si:H) to high-performance III-V group materials [9,10].

* Corresponding author.
E-mail address: ahmed.shaker@eng.asu.edu.eg (A. Shaker).

https://doi.org/10.1016/j.solmat.2023.112210
Received 26 September 2022; Received in revised form 23 January 2023; Accepted 28 January 2023
Available online 7 February 2023

However, the stability of a-Si:H under light coverage is restricted by the inevitable Staebler-Wronski effect [11] caused by the generation of deep defects that form recombination centers within the material [12]. Furthermore, despite having a high η over 30% [13], such as triple-junction solar cells with an η of 37.9% [14], III-V tandem cells' wide range of applications, such as concentrator PVs [15] or space applications [16], are constrained by their expensive and complex production procedures [17,18]. Similarly, despite Pb-based perovskites' outstanding performance in both single- and multi-junction solar cells, their high toxicity and intrinsic instability deflect researchers' attention away from exploring and investigating other environments' benign and stable counterparts [19]. As a result, developing wide bandgap, environmentally friendly, benign fabrication conditions and highly-efficient photovoltaic materials for future tandem solar cells are extremely important.

The preceding discussion clearly shows that Sb_2S_3 is one of the most appropriate top cell candidates for next-generation TSCs owing to its desired broad bandgap of 1.7 eV [20], intrinsic stability [21,22], non-toxicity, and less expensive constituent elements. As well, it has been theoretically shown that combining c-Si as a bottom sub-cell along with a top sub-cell whose material bandgap is 1.72 eV in a 2T TSC, an efficiency near 43% can be reached [23]. Consequently, Sb_2S_3, whose bandgap is 1.7 eV, can be a proper top cell partner combined with an optimal bottom cell like silicon in TSCs. A few studies have recently investigated Sb_2S_3 as a top cell in Si-based TSCs [24–26]. In 2016, Gao et al. [26] presented the first study on Sb_2S_3 as a top absorber, in which they deposited Sb_2S_3 on n-type Si-substrates using reactive sputtering at 350 °C. They concluded that Sb_2S_3 meets all requirements for a potential top sub-cell in silicon-based TSCs. Recently, a tandem cell based on Sb_2S_3 and Sb_2Se_3 as top and bottom cells was fabricated and an η of 7.93% was reported which surpasses the independently top Sb_2S_3 and bottom Sb_2Se_3 cells [27]. This experimental study proves the suitability of Sb_2S_3-based solar cell as a top cell of TSC and establishes a proof of concept.

The c-Si is an exceptional bottom cell candidate owing to its high efficiency, low bandgap of 1.12 eV, cost-competitiveness, natural abundance, non-toxicity, and robustness stability. In addition, it needs a top cell candidate with a bandgap of 1.6–1.9 eV, as reported in tandem device design [28]. Furthermore, recent improvements have brought c-Si solar cells' efficiency up to a record 26.8% [29,30], which is getting close to its theoretical efficiency limit of 29.56% [31]. Recent attempts have been made to achieve flexible PV cells by fabricating thin c-Si with substrates that are thinner than 50 μm [32–37]. The resultant thin c-Si cells shows excellent price competitiveness, high flexibility, and are, in addition, lightweight [34]. Moreover, thin c-Si cells can be fabricated using conventional silicon solar cell processing steps, which is expected to be commercialized quickly [37].

This paper proposes a TSC that combines Sb_2S_3 (1.7 eV) and thin film c-Si (1.12 eV) materials for the top and bottom sub-cells, respectively. Devices based on these materials are considered environmentally friendly solar cells, besides their low processing cost. Using all thin film layers results in flexible tandem that may be used in some applications like wearable electronics. Before the simulation of our proposed TSC, the two standalone sub-cells are calibrated versus experimental studies by applying the appropriate geometrical and physical parameters to validate the simulator. Next, the Sb_2S_3 top cell is optimized by designing the cell without HTL to avoid its organic issues and tuning the CBO between the ETL and the Sb_2S_3 absorber. Then, optimization steps are carried out to design the tandem for maximum possible efficiency. The first step is to optimize the ETL thickness and doping concentration. Further, the effect of changing the absorber defect density and the series resistance of the top cell on the TSC performance is investigated. Furthermore, the impact of varying the thicknesses of the top and bottom absorbers on the TSC is also explored to highlight the potential paths for promoting tandem efficiency.

Table 1
Basic parameters of the Sb_2S_3 and thin c-Si solar cell layers.

Parameters	Top Cell				Bottom Cell		
	FTO	TiO_2	Sb_2S_3	Spiro-OMeTAD	n+ Si	p Si	p+ Si
Thickness (μm)	0.5	0.03	0.125	0.2	0.1	20	0.2
Energy gap (eV)	3.5	3.2	1.7	3.17	1.12	1.12	1.12
Electron affinity (eV)	4	4.26	3.70	2.05	4.05	4.05	4.05
Relative permittivity	9	9	7	3	11.7	11.7	11.7
Electron mobility (cm^2/Vs)	20	20	0.8	2×10^{-4}	Default values		
Hole mobility (cm^2/Vs)	10	10	0.2	2×10^{-4}			
CB effective density of states (cm^{-3})	2.2×10^{18}	2×10^{18}	3×10^{19}	2.2×10^{18}	2.8×10^{19}	2.8×10^{19}	2.8×10^{19}
VB effective density of states (cm^{-3})	1.8×10^{19}	1.8×10^{19}	7×10^{19}	1.8×10^{19}	1×10^{19}	1×10^{19}	1×10^{19}
Shallow donor concentration N_D (cm^{-3})	2×10^{19}	1×10^{16}	–	–	1×10^{19}	–	–
Shallow acceptor concentration N_A (cm^{-3})	–	–	1×10^{15}	2×10^{19}	–	1×10^{15}	1×10^{20}
Reference	[54]	[55]	[56, 57]	[55]	[61]	[61]	[61]

2. Simulation methodology and device structure

2.1. Silvaco Atlas simulation methodology

A variety of software is available to investigate the performance of single junction or tandem solar cells, including Silvaco [38,39], SCAPS [3,40], AMPS [41], COMSOL [42], and wxAMPS [43]. In this study, the simulation study was performed using the Silvaco 2-D Atlas simulator. The operating principle of this simulation package is based on solving semiconductor transport equations along with Poisson's equation self-consistently through a defined grid [44]. The physical models inserted in Atlas must be properly selected. This study includes the primary physical models utilized to design a given TSC structure. SRH recombination is predominant in Sb_2S_3 cells because of the considerable recombination observed in Sb_2S_3 films with high defect density [45,46]. Besides, Auger recombination (AUGER) is enabled to account for recombination occurring in the regions of high doping. In addition, the Fermi-Dirac statistics (Fermi), optical recombination (OPTR), and concentration-dependent mobility (CONMOB) models are invoked.

Regarding the optics part, first, the optical intensity profiles inside the solar cell are estimated using an illuminated input source which is AM1.5. Then, photogeneration rates are calculated given the intensity. After that, the photogeneration rates are coupled into the continuity equations' generation terms. There are two models that are used concurrently at each bias in optoelectronic device simulation, namely the optical ray tracing and photogeneration models. Regarding the first model, the optical intensity is evaluated based on the real refractive index, while for the photogeneration model, the extinction coefficient is used to compute the carrier density [47,48]. The generation at a given point is computed by evaluating the integral of the generation rate as presented in the Supplementary Materials. More details about the modeling and numerical techniques can be found in Ref. [49].

It should be pointed out here that, to construct a 2T TSC, the interconnect between the two sub-cells should be Ohmic. This can be achieved by either a tunnel junction or thin layers in the order of 1 nm of Silver or Gold [50]. Also, the interconnection can be developed by an indium oxide layer which was experimentally validated to be effective

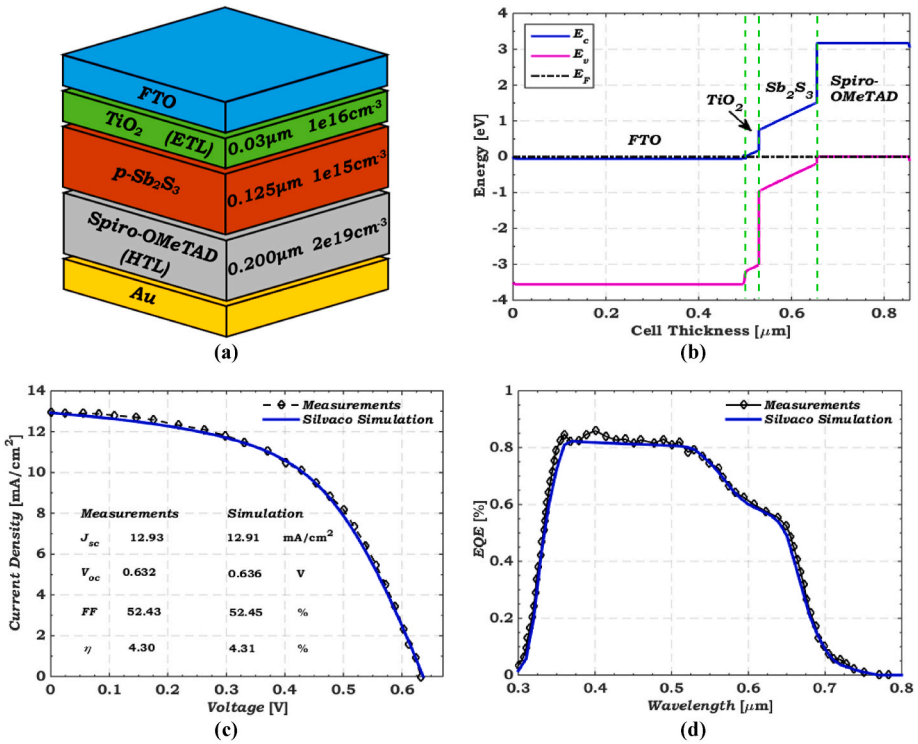

Fig. 1. (a) Basic structure including design parameters and (b) Energy band diagram after contact at the dark condition of Sb_2S_3-based cell. (c) Illuminated *J–V* and (d) *EQE* curves of both simulated and experimental Sb_2S_3 cells [53].

for both electrical and optical behavior [51]. In our simulation, a lumped resistance is added as an interlayer such that the current flows across the two sub-cells of the TSC without substantial constraint [52].

2.2. Calibration of two sub-cells

A heterojunction top Sb_2S_3 cell having an n-i-p structure is given presented on a practical configuration of a fabricated solar cell that contains the same transport layer materials [53]. A lightly doped

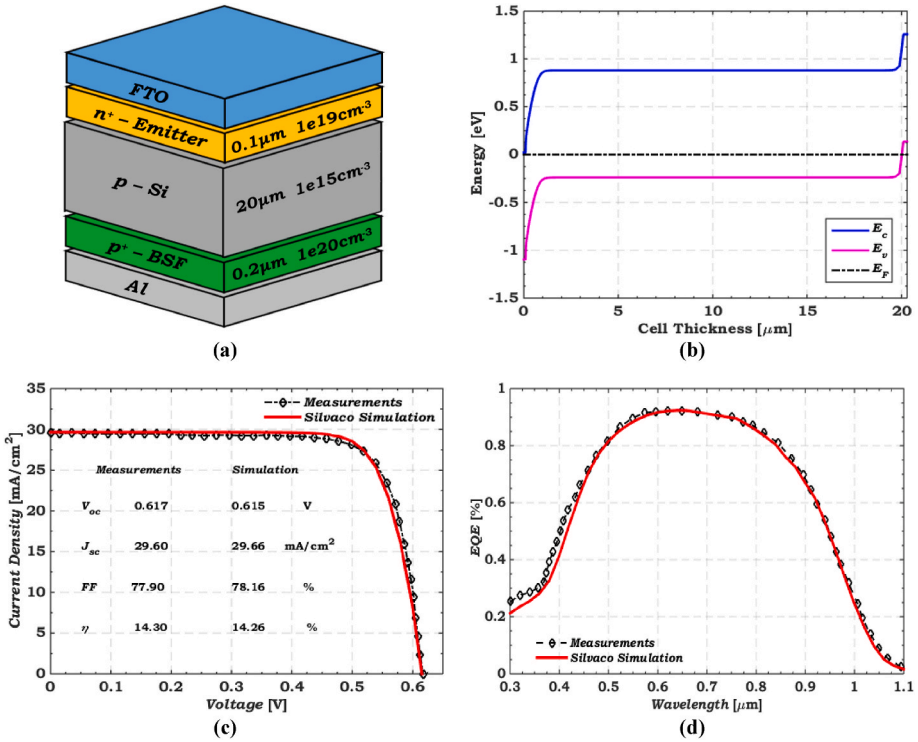

Fig. 2. (a) Basic structure including design parameters, and (b) Energy band profile after contact at the dark condition of a thin c-Si cell. (c) Illuminated *J–V* and (d) *EQE* curves of both simulated and experimental thin c-Si cells [60].

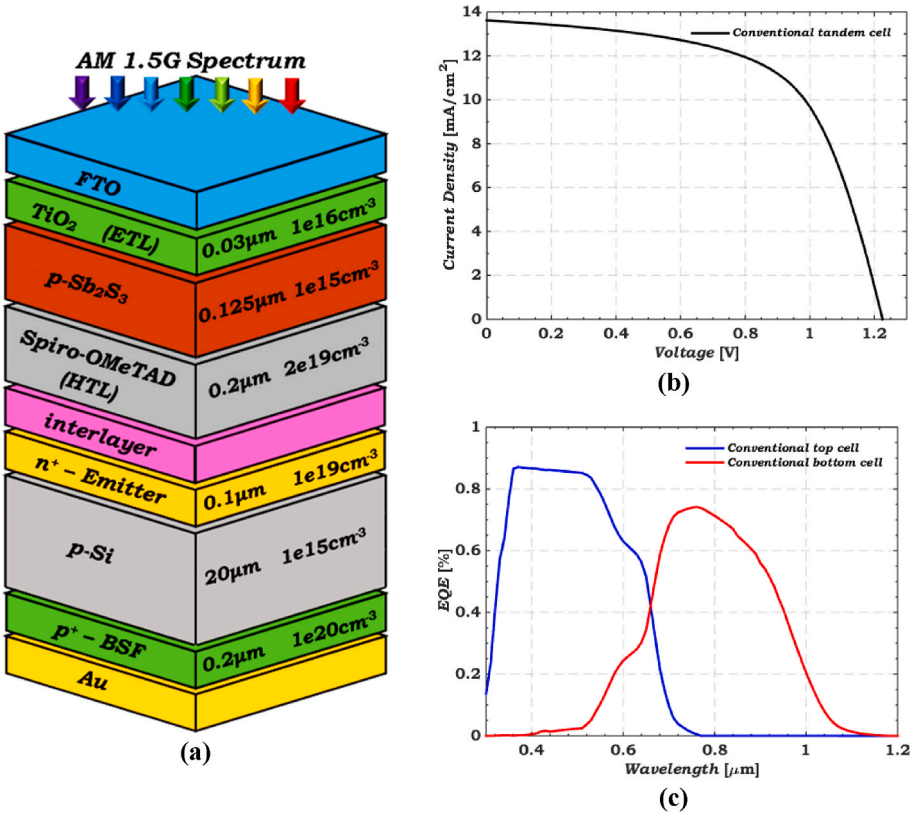

Fig. 3. (a) Schematic illustration indicating the design parameters, (b) the illuminated *J–V* characteristics, and (c) *EQE* curve of a conventional Sb_2S_3/Si tandem cell.

p-Sb_2S_3 film is sandwiched between lightly doped n-TiO_2 and p^+-Spiro-OMeTAD layers to create a heterojunction solar cell and extract photoexcited electron-hole pairs. The experimental steps of the fabricated Sb_2S_3 are performed firstly by preparing a diluted CS_2 in an ethanol precursor solution and followed by dissolving the low-cost Sb_2O_3 and Sb-source in the solution. The produced Sb_2S_3 film had a lateral grain size up to 12 μm which is achieved through spin-coating and annealing at 300 °C for 2 min. More details about the processing steps and conditions as well as the electrical characterization are found in Ref. [53].

Fig. 1(a) and (b) depict the top cell's device design and energy band diagram. The key parameters of cell layers derived from previously published studies are summarized in Table 1 [54–58]. In addition, Defect parameters in the cell layers and at the interfaces (TiO_2/Sb_2S_3 and Sb_2S_3/Spiro-OMeTAD) are presented in Table S1. The work function of the FTO (transparent conducting top contact) is set to 4 eV, whereas that of the rear Au contact is taken to be 5.1 eV. A parasitic series resistance (R_s) is fitted at 10 Ω cm^2 to match the experimental results [59]. Upon utilizing the listed parameters, the illuminated current density-voltage (*J-V*) along with the external quantum efficiency (*EQE*) characteristics of both simulated and experimental Sb_2S_3 cells [59] are presented in Fig. 1(c) and (d). The simulated cell gives: (J_{sc} = 12.91 mA/cm^2, V_{oc} = 0.636 V, *FF* = 52.45%, and η = 4.31%). These PV parameters well match the reported experimental parameters, as shown in the inset of Fig. 1(c), implying that the simulation model employed in Silvaco Atlas software has been validated.

A homojunction bottom c-Si cell having a n^+-p-p^+ configuration, on the other hand, is calibrated against the experimental thin c-Si cell, yielding the following performance parameters: (J_{sc} = 29.60 mA/cm^2, V_{oc} = 0.617 V, *FF* = 77.90%, and η = 14.30%) [60]. The first step in the experimental processes of the fabricated c-Si bottom cell was firstly to etch a 380 μm Czochralski grade n-type crystalline silicon wafer to produce a 20 μm thin c-Si substrate. The emitter and back surface field (BSF) regions were then created by employing the spin-on-dopant technique. Finally, Al electrodes were defined by using a thermal evaporator. More details about the manufacturing and characterization steps can be found in Ref. [60].

Fig. 2(a) and (b) depict the cell design and energy band diagram of the n^+pp^+-Si bottom cell. The essential parameters of cell layers are summarized in Table 1 [61]. In addition, carrier mobility and carrier lifetime within cell layers are based on default values incorporated in Atlas. The illuminated *J-V* and *EQE* characteristics of both simulated and experimental c-Si cells are obtained as presented in Fig. 2(c) and (d). The cell gives the following performance factors: (J_{sc} = 29.66 mA/cm^2, V_{oc} = 0.615 V, *FF* = 78.16%, and η = 14.26%), indicating an insignificant difference between our simulation results and experimental data [60] and also validating the simulation model employed in Silvaco Atlas software.

2.3. Conventional Sb_2S_3/Si tandem cell

This subsection presents a 2T monolithic conventional Sb_2S_3/Si tandem cell. Fig. 3(a) depicts the cell's suggested structure, indicating its design parameters. As mentioned herein, in a 2T monolithic tandem cell, the two cells are coupled through a tunnel junction [62,63] or an interface layer (transparent conductive oxide or a very thin metallic film) [64–66] that performs as a recombination layer. The current flowing in a TSC is controlled by the smaller current transporting through either the front or the back sub-cell. Therefore, the current matching situation must be provided to minimize the current loss. Additionally, a broad bandgap absorber is required regarding the top sub-cell, as explained herein. Therefore, our design adopts an Sb_2S_3 solar cell having a bandgap of 1.7 eV as a front cell along with the thin c-Si. The conventional TSC is simulated using Atlas under AM1.5G illumination, and the simulation results are displayed in Fig. 3(b) and (c). The cell performance metrics are (J_{sc} = 13.61 mA/cm^2, V_{oc} = 1.23 V, *FF* = 60.55%, and η = 10.10%). The V_{oc} of the TSC is nearly equal to the sum of V_{oc} of the individual sub-cells, while its current is governed by the cell

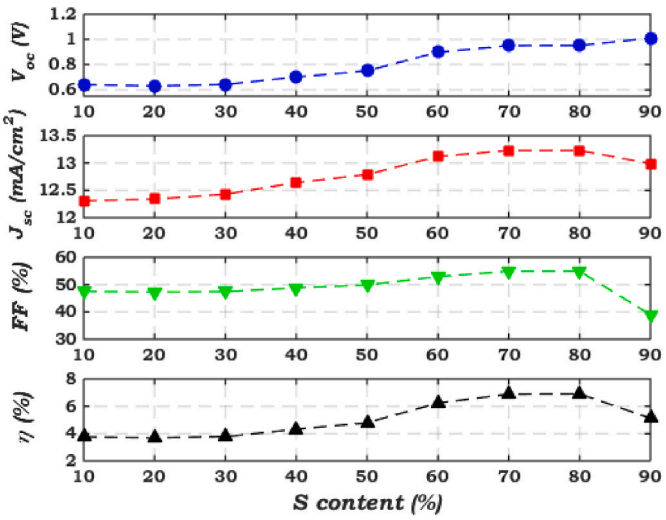

Fig. 4. Performance parameters of $ZnO_{1-x}S_x$ with different S content.

with the smallest current among the two cells.

3. Results and discussion

As seen in the previous section, there is a significant deterioration in tandem performance which is attributed to recombination losses due to bulk defects in the Sb_2S_3 absorber layer; thus, V_{oc} is reduced, which is the dominant bottleneck of high-performance antimony chalcogenide solar cells [67]. Furthermore, interface defects are typically caused by a mismatch lattice between the TiO_2 buffer layer and the Sb_2S_3 absorber layer. Thus, the recombination defects at the Sb_2S_3/TiO_2 interface [68] would sacrifice the photocarriers. Therefore, the Sb_2S_3 top cell has to be optimized, especially for conduction band offset (CBO), before incorporating it in a 2T monolithic Sb_2S_3/Si tandem cell.

3.1. Initial enhancement of Sb_2S_3 top cell

The principal role of ETL and HTL is to ease the extraction of photogenerated carriers from the absorber layer to both contacts. Nonetheless, interface defects at the Sb_2S_3 interfaces promote electron and hole recombination and degrade overall solar cell performance [69,70]. To improve Sb_2S_3 top cell performance while avoiding the technological and financial challenges associated with HTL, we continue to design the cell without an HTL and with a ternary compound ETL. So, the cell is designed as an HTL-free cell meaning that it is an np heterojunction instead of the conventional nip structure. This configuration implies that the p-absorber (Sb_2S_3 in our case) will serve as both an absorber and as a hole transporting layer without the need for an extra layer.

Since the selectivity of the ETL affects the solar cell performance, primarily characterized by energetics and transport features such as band alignment and charge carrier mobility, perfect ETL can significantly reduce interfacial recombination. An optimum CBO can be obtained by performing a suitable band alignment at the ETL/Sb_2S_3 interface [71]. CBO is a crucial factor in determining V_{oc} and cell efficiency, and it is described as

$$CBO = \Delta E_c = \chi_{absorber} - \chi_{ETL} \quad (1)$$

At the interface, there are three options for band alignment. The first is a cliff-like band offset by a negative CBO value. A positive CBO spike-like band offset is the second encountered condition. Finally, a flat band condition derives from the third potential situation for a zero CBO. The cliff-like band offset at the interface is well known to cause severe interface recombination [72]. Furthermore, a substantial spike-like band offset, which signifies a CBO greater than 0.3 eV, may inhibit interface carrier transfer [72]. Generally, a flat band or a slight spike-like band offset is preferable in thin film solar cells [73].

Herein, we apply the ternary compound $ZnO_{1-x}S_x$ as an ETL to tune

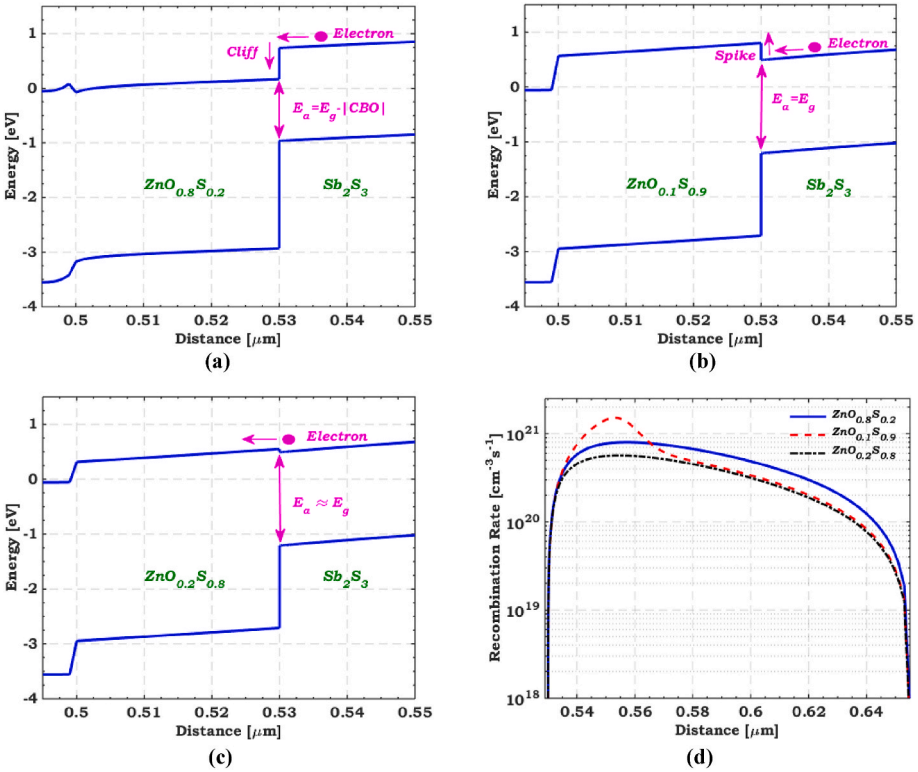

Fig. 5. Energy band diagrams of three various cases of CBOs (a) A cliff-like band appears regarding $ZnO_{0.8}S_{0.2}/Sb_2S_3$, (b) a spike-like band occurs regarding $ZnO_{0.1}S_{0.9}/Sb_2S_3$ and (c) almost flat band regarding $ZnO_{0.2}S_{0.8}/Sb_2S_3$. (d) recombination rate along the Sb_2S_3 absorber layer.

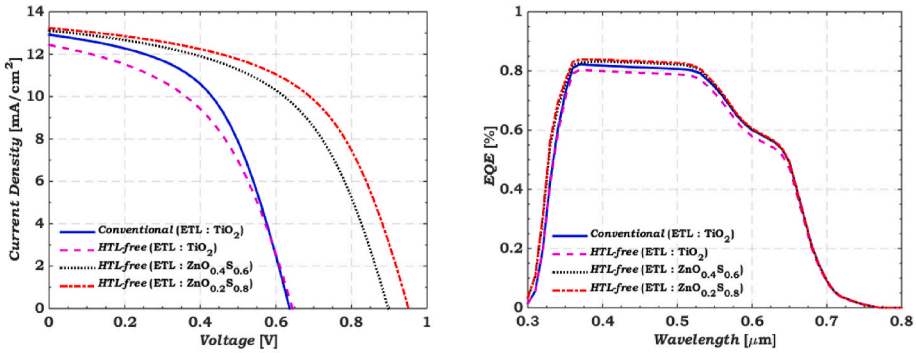

Fig. 6. A comparison between (a) the illuminated *J–V* and (b) *EQE* curves for the initial and HTL-free cells using TiO_2, $ZnO_{0.4}S_{0.6}$, and $ZnO_{0.2}S_{0.8}$ as ETLs.

the interface band alignment. $ZnO_{1-x}S_x$ and bilayer $ZnO_{1-x}S_x$/CdS ETLs have been used in antimony chalcogenide-based solar cells with promising results [74]. The variation of bandgap energy (E_g), and electron affinity (χ) of $ZnO_{1-x}S_x$ with sulfur (S) content were extracted from the literature [75], as illustrated in Fig. S1(a) (see Supplementary Materials file). In addition, Fig. S1(b) (see Supplementary Materials file) presents the variation of $ZnO_{1-x}S_x$ CBO with S content. Moreover, the refractive index *n'* and extinction coefficient κ dependency on wavelength of $ZnO_{1-x}S_x$ were obtained from experimental data [76,77]. Fig. 4 depicts the response of performance metrics to S content. As illustrated in Fig. 4, all performance parameters almost follow the same trend for S content values less than 80%. They gradually increase with increasing S content and almost saturate above S = 60%. Although V_{oc} increases with S > 80%, other parameters decrease significantly in *FF*. The maximum η is attained when S = 80%, resulting in almost zero CBO and hence a flat band offset. As a result, $ZnO_{0.2}S_{0.8}$ is a suitable material for use as ETL in the proposed HTL-free sub-cell.

For a physical explanation of the results shown in Fig. 4, representative band diagrams of three distinct CBOs are plotted, as well as the recombination rate along the absorber, as illustrated in Fig. 5. The first CBO is −0.57eV for $ZnO_{0.8}S_{0.2}$, which shows a cliff-like band in Fig. 5(a). The second one, shown in Fig. 5(b), is 0.31eV for $ZnO_{0.1}S_{0.9}$ with a spike-like band. The last is 0.06eV for $ZnO_{0.2}S_{0.8}$, which has a nearly flat band, as depicted in Fig. 5(c). Although the cliff band case, depicted in Fig. 5 (a), does not impede the extraction of photogenerated electrons from the absorber layer to the front metal, it affects the activation energy associated with carrier recombination. In this case, the activation energy (E_a) is less than the absorber bandgap (E_g), and thus the primary recombination process within the solar cell is interfacial recombination losses [71,78]. Remarkably, E_a has a direct influence on V_{oc}; thus, V_{oc} is decreased for S content values less than 70% (negative CBO values), as illustrated in Fig. 4. Conversely, a spike is formed at the $ZnO_{0.1}S_{0.9}/Sb_2S_3$ interface, as shown in Fig. 5(b). This spike obstructs the extraction of photoexcited electrons from the absorber layer toward the front metal. When the spike is sufficiently low, it becomes ineffective, allowing electrons to flow properly towards the contact. However, as in the $ZnO_{0.1}S_{0.9}/Sb_2S_3$ case, the spike is too high, significantly altering the regular flow of electrons toward the front metal. Consequently, the cell's equivalent series resistance rises, resulting in fill factor deterioration (see Fig. 4) [79–81]. Finally, a flat band is formed at the $ZnO_{0.2}S_{0.8}/Sb_2S_3$ interface, as shown in Fig. 5(c). In this case, no barrier obstructs the carrier flow, and E_a is not compromised, resulting in a higher V_{oc} value. As a result, the optimum case is the flat band case. The recombination rate of three situations is depicted in Fig. 5(d) to confirm these findings. $ZnO_{0.2}S_{0.8}$ has the lowest recombination rate along the absorber layer. Therefore, with η = 6.90%, $ZnO_{0.2}S_{0.8}$ is the best selection for the ETL in the proposed HTL-free cell.

In addition, Fig. 6(a) and (b) depict a comparison between the illuminated *J–V* and *EQE* curves concerning the initial and the HTL-free cells using TiO_2, $ZnO_{0.4}S_{0.6}$, and $ZnO_{0.2}S_{0.8}$ as ETLs. Their performance metrics are listed in Table 2. The results show that when the ETL is appropriately designed, there is a significant improvement. A percentage rise of about 60% is yielded when $ZnO_{0.2}S_{0.8}$ is designed as an ETL in the proposed HTL-free cell when compared to the initial conventional cell.

Table 2
A comparison between the solar cell performance metrics concerning the initial and HTL-free cells when utilizing TiO_2, $ZnO_{0.4}S_{0.6}$, and $ZnO_{0.2}S_{0.8}$ as ETLs.

Structure	Conventional TiO_2	HTL-free TiO_2	HTL-free $ZnO_{0.4}S_{0.6}$	HTL-free $ZnO_{0.2}S_{0.8}$
V_{oc} (V)	0.636	0.644	0.897	0.951
J_{sc} (mA/cm^2)	12.91	12.44	13.12	13.23
FF (%)	52.45	47.46	52.95	54.88
η (%)	4.31	3.80	6.23	6.90

3.2. Tandem cell optimization

This subsection presents the following optimization steps for a 2T monolithic Sb_2S_3/Si TSC. First, the impact of thickness and doping of the top cell ETL on the tandem performance is studied. Then, the effect of changing the absorber defect density and the series resistance of the top cell on the TSC performance is investigated. Furthermore, we investigated the impact of top and bottom absorber thicknesses on TSC working metrics. Finally, we inspected for the current matching point to get the maximum available η. Fig. 7 depicts the proposed structure utilized in the Sb_2S_3/Si tandem cell optimization steps.

3.2.1. Thickness and doping of the top cell ETL

Changing the conductivity of different solar cell layers is critical in cell design. The doping process, which can be p-type or n-type depending on the type of dopants, can regulate conductivity. Fig. 8 describes the variation in tandem performance factors with variation in doping concentration and thickness of the top cell ETL. The doping density was changed from 1×10^{16} to 1×10^{19} cm^{-3} and the thickness was varied from 27 to 33 nm, while other parameters were fixed to investigate the tandem performance. As indicated in the figure, all performance parameters follow the same trend for different ETL thicknesses. They gradually increase and become constant beyond a concentration of 2×10^{18} cm^{-3}. Furthermore, the best tandem performance is obtained with a 30 nm ETL thickness, whereas other thicknesses significantly degrade performance. The best performance is chosen when the thickness and doping of the ETL are 30 nm and 5×10^{18} cm^{-3}, respectively. The TSC metrics, in this case, are (J_{sc} = 14.19 mA/cm^2, V_{oc} = 1.55 V, *FF* = 63.50%, and η = 14.15%).

To physically interpret this enhancement, the electric field

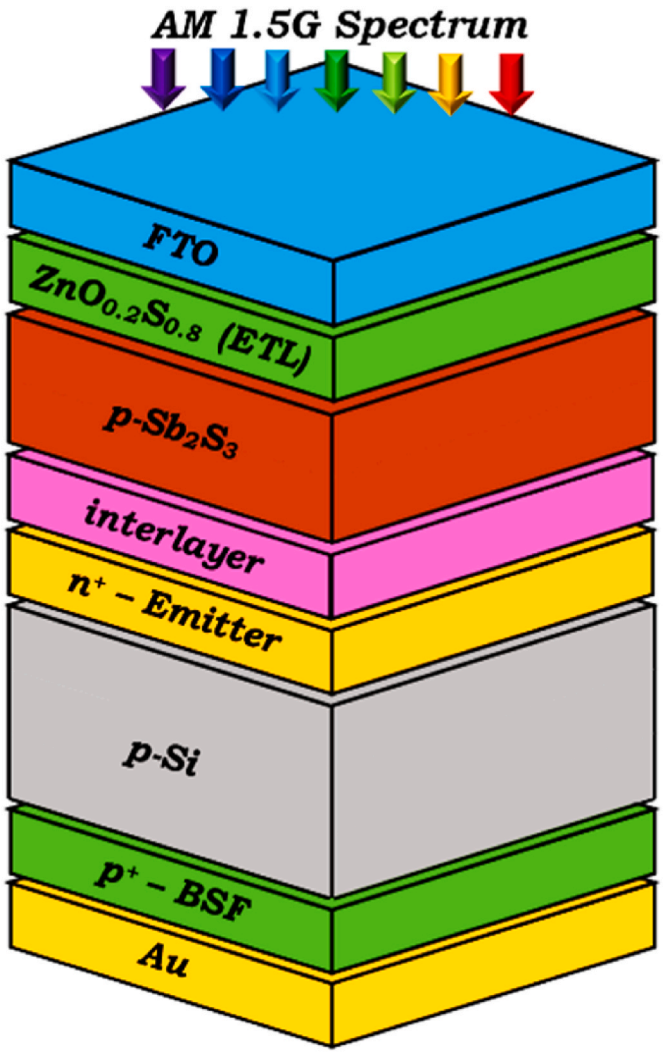

Fig. 7. The proposed structure utilized in the Sb_2S_3/Si tandem cell optimization steps.

distribution, and the spatial distribution of the electron conductivity at the maximum power point (MPP) before and after ETL optimization are plotted and shown in Fig. 9. The energy band diagram is also illustrated in Fig. S2 in the Supplementary Materials file. As illustrated in Fig. 9(a), increasing $ZnO_{0.2}S_{0.8}$ doping increases the electric field substantially. Moreover, to comprehensively represent the carrier separation, the electron conductivity is plotted as seen in Fig. 9(b). Carrier conductivity is considered a key factor that controls the carrier separation in the solar cell [82]. As clarified in Fig. 9(b), increasing $ZnO_{0.2}S_{0.8}$ doping increases the electron conductivity in the $ZnO_{0.2}S_{0.8}$ and the $ZnO_{0.2}S_{0.8}/Sb_2S_3$ interface resulting in faster separation of photogenerated carriers, lower recombination rates, and improved cell performance. So, the enhancement resulting from the high doping is accomplished due to the concurrent improvement of both the electric field as a driving force and the conductivity as a source of current magnitude.

3.2.2. Defect density of the top cell absorber

Fig. 10 depicts the change in tandem cell performance metrics with the variation in bulk defect density of the top cell absorber. The defect density varies from 1×10^{12} to 5×10^{16} cm^{-3} while maintaining the other parameters unchanged. As the figure shows, all performance parameters follow the same trend. They are constantly up to about 1×10^{15} cm^{-3} and then gradually degraded when increasing the defect density beyond this value. The defect density of 1×10^{14} cm^{-3} is selected and output parameters, in this case, are ($J_{sc} = 14.57$ mA/cm^2, $V_{oc} = 1.61$ V, $FF = 76.43\%$, and $\eta = 17.86\%$). This value of defect density was already reported in the literature upon the enhancement of fabrication methods [83,84]. This significant improvement in cell performance with decreasing defect density is attributed to decreased carrier recombination (which means higher diffusion lengths), as shown in Fig. 11. The figure demonstrates the recombination rate (R) behavior for the absorber layer with various defect densities under short-circuit conditions. In addition, the generation rate (G) is depicted to give a comparative figure. As expected, as trap density grows, the recombination rate climbs dramatically, indicating poor performance. Several approaches, including trap state passivation in the Sb_2S_3 absorber layer, post-annealing and interlayer passivation, have been used to reduce defect density and increase carrier lifetime and V_{oc} [85].

3.2.3. Series resistance of the top cell

Solar cells' parasitic resistances lead to resistive effects, lowering their overall performance. The resistance of the cell layers, as well as

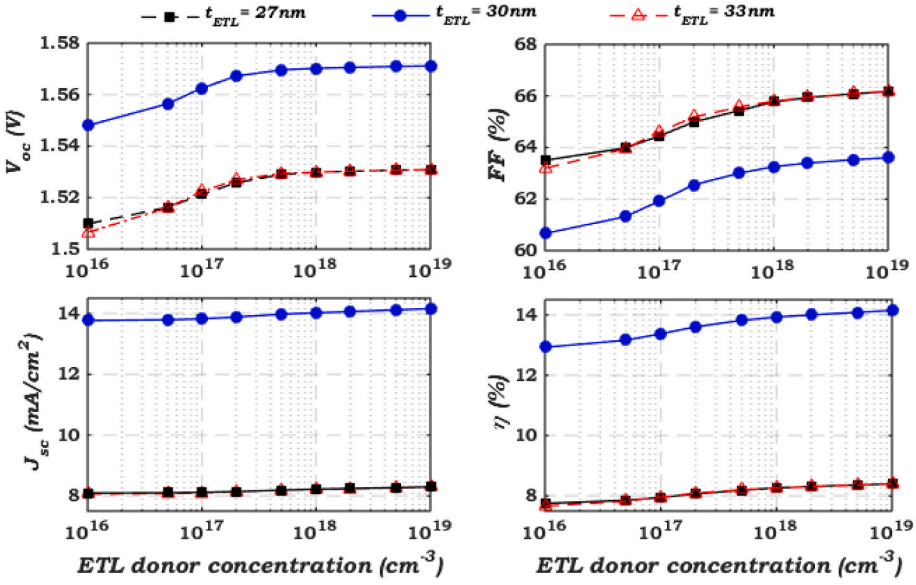

Fig. 8. Variation in tandem performance parameters depending on the variation of an ETL doping concentration and thickness.

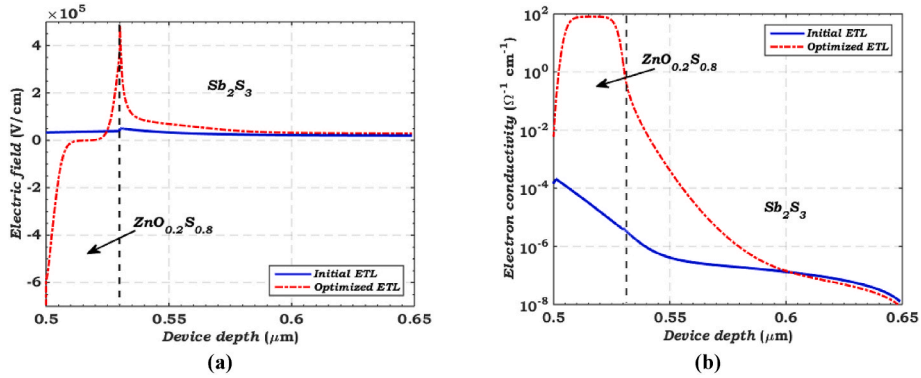

Fig. 9. (a) The electric field distribution, and (b) the spatial distribution of the electron conductivity at the MPP before and after optimization of the top cell ETL.

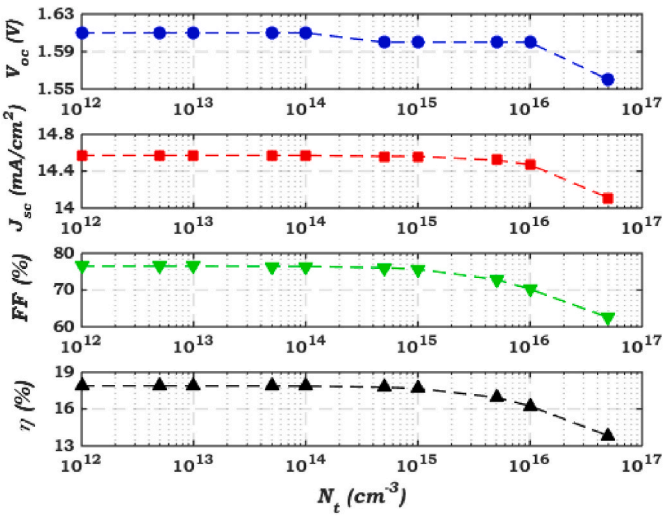

Fig. 10. Variation in tandem performance parameters depending on the variation of the absorber defect density.

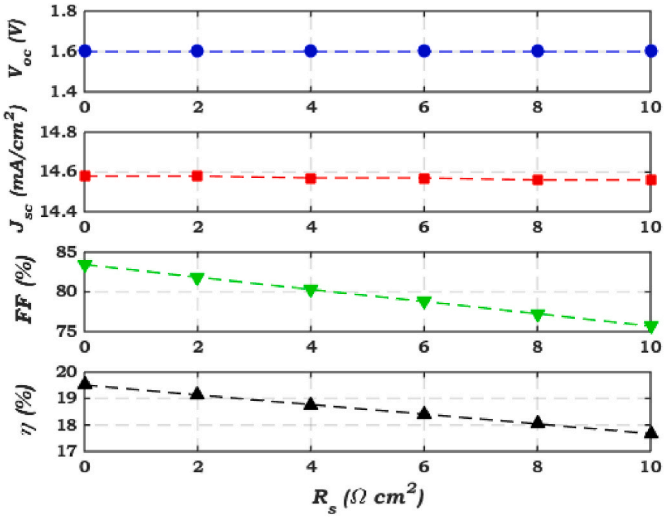

Fig. 12. Variation of tandem performance parameters for different values of series resistance.

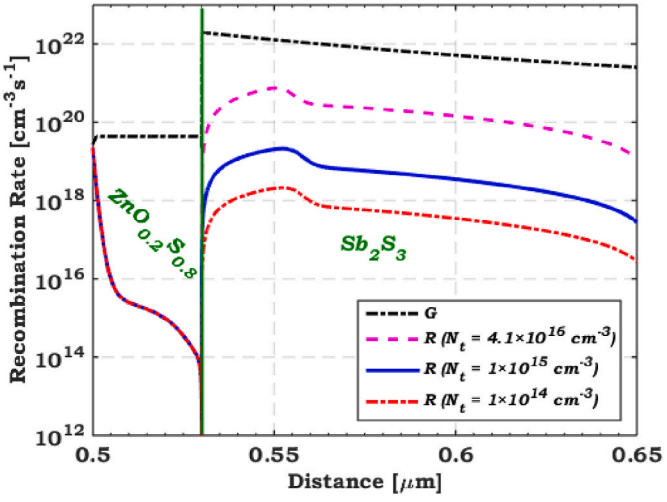

Fig. 11. The generation and recombination rate behavior drawn at the illuminated short-circuit condition for the top absorber layer.

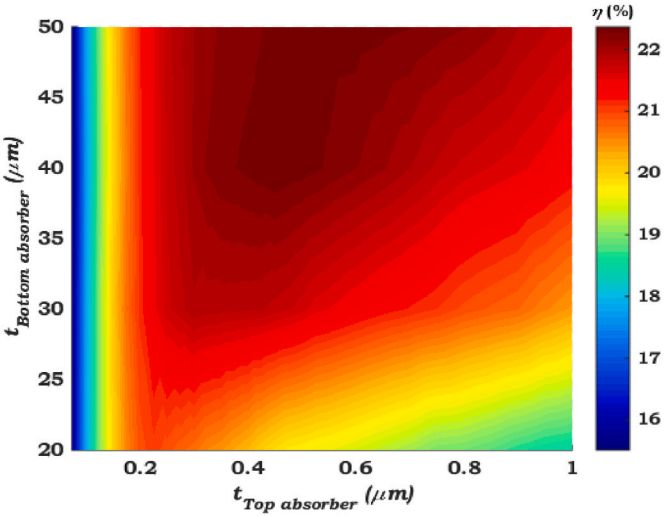

Fig. 13. Contour graph of TSC efficiency dependency on the thickness of top and bottom absorber layers.

metal contact resistances, cause the series resistance (R_s) to appear. The fill factor (*FF*) is the most influenced factor by R_s. Fig. 12 depicts the variation in tandem performance parameters as a function of R_s. When R_s is increased from 0 (ideal case) to 10 Ω cm^2, the V_{oc} and J_{sc} remain nearly unaffected while the *FF* decreases, resulting in efficiency reduction. The decrease in *FF* is due to higher R_s dissipating more power. These results confirmed that R_s should be kept low to attain an efficient

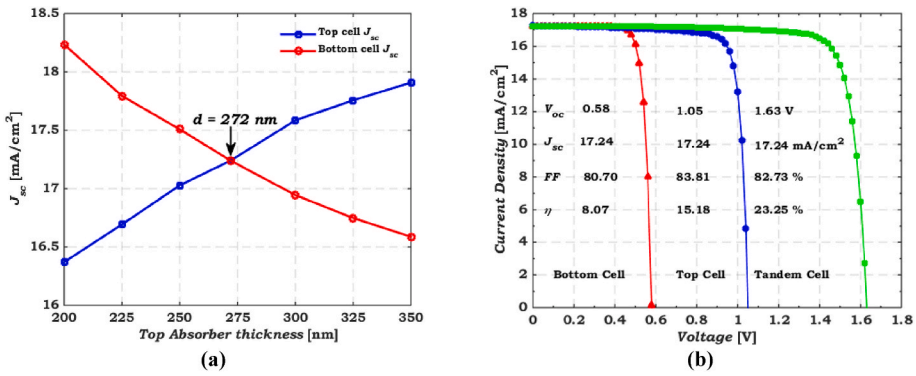

Fig. 14. (a) J_{sc} of front- and rear-cells vesus d of top cell absorber film. (b) J-V characterisitcs of tandem-, front-, and back-cells under current matching point.

Table 3
A comparison between the performance metrics for Sb_2S_3/Si tandem cells under various optimization steps.

Cell Structure	J_{sc} (mA/cm^2)	V_{oc} (V)	*FF* (%)	η (%)
Conventional	13.61	1.23	60.55	10.10
Optimized CBO	13.84	1.55	60.63	12.98
Optimized ETL	14.19	1.57	63.50	14.15
Optimized N_t	14.57	1.61	76.43	17.86
Optimized R_s	14.57	1.61	83.44	19.51
Optimized t_{abs}	16.47	1.62	83.88	22.31
Final Optimization	17.24	1.63	82.73	23.25

cell. The ideal case is chosen to inspect the limit of possible higher efficiencies utilized by the tandem cell. The solar cell metrics, in this case, are (J_{sc} = 14.58 mA/cm^2, V_{oc} = 1.61 V, *FF* = 83.44%, and η = 19.51%).

3.2.4. Thickness of top and bottom absorber layers

Fig. 13 represents a contour graph of TSC efficiency dependence on the thickness of both top and bottom absorber layers. To investigate device performance, the thickness of the top absorber was increased from 75 up to 1000 nm and that of the bottom absorber was increased from 20 to 50 μm while the other parameters remained constant. As obvious from Fig. 13, there is an inconsiderable effect on η as the thickness of the rear absorber grows from 30 to 50 μm and that of the front absorber raises from 200 to 1000 nm. As the bottom absorber thickness falls below 150 nm, the efficiency gradually decreases from 20% to 15%. Furthermore, there is no change in η as the bottom absorber thickness changes from 20 to 50 μm, while the thickness of the bottom absorber layer remains constant below 150 nm. The best performance is chosen when thicknesses of top and bottom cells are 200 nm and 30 μm, respectively. The solar cell metrics, in this case, are (J_{sc} = 16.47 mA/cm^2, V_{oc} = 1.62 V, *FF* = 83.88%, and η = 22.31%).

3.2.5. Current matching point

In this part, the top cell's absorber thickness (d) is changed from 200 to 350 nm, while the bottom c-Si thickness is fixed at 30 μm. Fig. 14(a) displays the J_{sc} variation of the front and rear sub-cells against the thickness of the Sb_2S_3 absorber layer in the front cell, indicating considerable dependence on d. As d becomes thicker, J_{sc} of the top sub-cell increases, and that of the bottom sub-cell, in turn, declines. The reason is that the thicker the front cell is, the more photon absorption occurs, implying lesser transferred light to the bottom sub-cell. A current matching point happens at J_{sc} = 17.24 mA/cm^2 and d = 272 nm. Under this condition, the performance of the Sb_2S_3/c-Si tandem cell has been simulated where the corresponding J-V curves of tandem, top, and back cells are represented in Fig. 14(b). The maximum value of J_{sc} is 17.24 mA/cm^2 with V_{oc} = 1.63 V and η = 23.25% for the TSC. The values of V_{oc} = 1.63 V and η = 23.25% are approximately equal to the sum of those of the top cell (V_{oc} = 1.05 V and η = 15.18%) and bottom cell (V_{oc} = 0.58 V and η = 8.07%), signifying minimum energy loss.

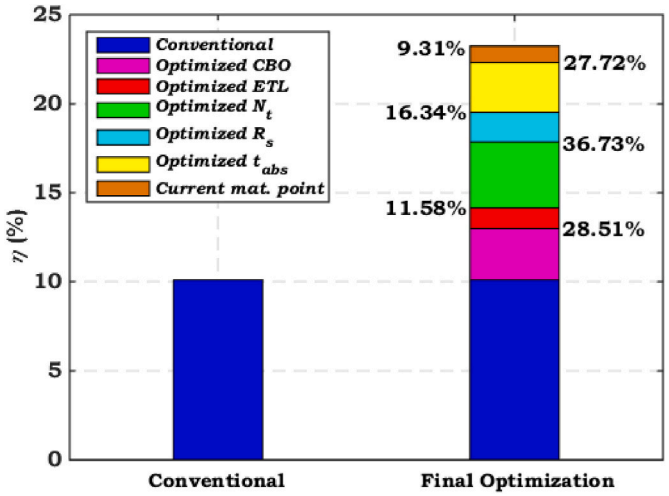

Fig. 15. Calculated efficiency improvements for different cases of tandem cells showing the enhancement relative percentage.

The performance parameters for Sb_2S_3/Si tandem cells under various optimization steps are presented in Table 3. Further, Fig. 15 depicts η of the various optimization steps and the improvement percentage in η over the previous step. According to the results, the most significant effect parameters among the various factors are the optimization of N_t and CBO, which provide 36.73% and 28.51% enhancement relative percentages, respectively. This highlights the significance of trap state passivation in the Sb_2S_3 film and CBO engineering in reducing defect density and avoiding interface recombination, negatively impacting cell performance. In addition, Fig. 16 displays the illuminated J-V characteristics and *EQE* curves of a conventional and a final optimized tandem cell. This considerable improvement in tandem performance is attributed to the overall optimization steps, which attained a maximum η of 23.25% with a relative percentage enhancement of 130.20% compared with the initial TSC.

Moreover, we investigated the effect of bottom absorber thickness by extending it to 50 μm, which is the limit for thin film silicon solar cells [32–35]. In this context, the current matching point is evaluated by engineering the top cell thickness to get the best tandem performance, as illustrated in Fig. S3 in the Supplementary Materials file. In this case, the top absorber thickness is varied from 275 to 475 nm resulting in current matching point at d = 375 nm. Under this condition, the performance metrics of the optimized TSC are (J_{sc} = 18.04 mA/cm^2, V_{oc} = 1.64 V, *FF* = 82.41%, and η = 24.34%).

Finally, we provide a comparison between our optimized TSC and other tandem candidates, as shown in Table 4. Some of the reported

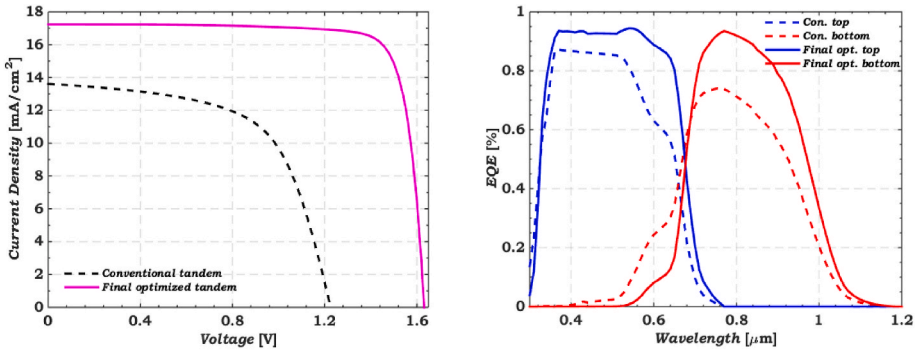

Fig. 16. A comparison between (a) illuminated *J–V* and (b) *EQE* curves of a conventional and a final optimized tandem cell.

Table 4
A state-of-art comparison between performance parameters of Sb_2S_3/Si tandem cell and state-of-the-art multi-junction solar cells stated in the literature.

Material	Tandem configuration	Method	J_{sc} (mA/cm^2)	V_{oc} (V)	*FF* (%)	η (%)	Reference
Lead-based Perovskite/Si	2T	Exp.	20.24	1.979	81.2	32.5	[90]
Lead-based Perovskite/Si	2T	Exp.	20.47	1.913	79.8	31.3	[29]
$GaAs_{0.75}P_{0.25}$/Si	2T	Exp.	17.34	1.732	77.70	23.4	[29]
Lead-based Perovskite/CIGS	2T	Exp.	19.24	1.768	72.9	24.2	[29]
Sb_2S_3/Sb_2Se_3	4T	Exp.	–	–	–	7.93	[27]
Lead-based Perovskite/Si	4T	Exp.	–	–	–	28.3	[91]
Lead-free Perovskite/Si	2T	Sim.	16.01	1.76	86.7	24.4	[92]
Lead-based Perovskite/Si	2T	Sim.	18.81	2.01	83.61	31.67	[93]
Lead-based Perovskite/CIGS	2T	Sim.	20.49	1.81	81.8	30.5	[94]
Sb_2S_3/Si (t_{Si} = 30 μm)	2T	Sim.	17.24	1.63	82.73	23.25	This work
Sb_2S_3/Si (t_{Si} = 50 μm)	2T	Sim.	18.04	1.64	82.41	24.34	This work

tandem cells are based on experimental investigations, while others are computed numerically, as illustrated in the table. The efficiency of all Antimony Chalcogenide TSC has not exceeded the limit of 8% according to experimental efforts till now. Moreover, most of tandem cells with lead-based perovskite top cell give higher efficiencies than our proposed thin film tandem cell; however, the toxicity of such tandems is a serious issue that limits their use. One of the main limitations of the Sb_2S_3 is the high level of bulk defects. This limitation has been investigated by many research studies [86–88]. It is also obvious from the high value of the series resistance that this is a serious limitation of the cell. However, by developing appropriate fabrication methods [21,53,83,84,89], both limitations can be alleviated to push the efficiency and thereby enhance the overall performance of the tandem cells including Sb_2S_3.

4. Conclusion

In our work, a 2T monolithic thin film Sb_2S_3/Si TSC is presented. The proposed design utilizes Sb_2S_3 having a 1.7 eV bandgap as a front cell, while thin c-Si with a 1.12 eV bandgap is incorporated as the bottom cell. The calibrated standalone cells versus experimental data give an η of 4.31% and 14.26% regarding the top and bottom sub-cells, respectively. Then, the Sb_2S_3 top cell is optimized by designing an HTL-free np heterojunction cell and tuning CBO between the ETL and the Sb_2S_3 absorber. Then, we optimize the TSC by inspecting the appropriate ETL thickness and doping concentration. Also, the impact of changing the absorber defect density and the series resistance of the top cell on the TSC performance is investigated to get the maximum available η. At defect density of 1×10^{14} cm^{-3} and $R_s = 0$, the efficiency of a 2T monolithic TSC is improved from 10.10% to 19.51%. Additionally, we have inspected the consequence of the top absorber thickness on TSC performance parameters for two cases of bottom absorber thickness (t_{Si}). At the designed matching point for each case, the optimum efficiency was achieved giving $J_{sc} = 17.24$ mA/cm^2, and $\eta = 23.25\%$ for $t_{Si} = 30$ μm, while $J_{sc} = 18.04$ mA/cm^2, and $\eta = 24.34\%$ for $t_{Si} = 50$ μm. These results can provide potential routes for advancing low-cost, environmentally friendly, and efficient thin film tandem solar cells which can be used in flexible applications.

CRediT authorship contribution statement

M. Okil: Writing – review & editing, Writing – original draft, Validation, Software, Methodology, Conceptualization. **Ahmed Shaker:** Writing – review & editing, Validation, Software, Methodology, Investigation, Conceptualization. **Ibrahim S. Ahmed:** Visualization, Validation, Methodology, Investigation. **Tarek M. Abdolkader:** Writing – review & editing, Validation, Supervision, Methodology, Investigation, Conceptualization. **Marwa S. Salem:** Writing – review & editing, Visualization, Resources, Methodology, Conceptualization.

Declaration of competing interest

The authors declare that they have no known competing financial interests or personal relationships that could have appeared to influence the work reported in this paper.

Data availability

Data will be made available on request.

Appendix A. Supplementary data

Supplementary data to this article can be found online at https://doi.org/10.1016/j.solmat.2023.112210.

References

[1] M.A. Green, Commercial progress and challenges for photovoltaics, Nat. Energy 1 (2016), https://doi.org/10.1038/nenergy.2015.15.

[2] C. Battaglia, A. Cuevas, S. De Wolf, High-efficiency crystalline silicon solar cells: status and perspectives, Energy Environ. Sci. 9 (2016) 1552–1576, https://doi.org/10.1039/c5ee03380b.

[3] W. Abdelaziz, A. Zekry, A. Shaker, M. Abouelatta, Numerical study of organic graded bulk heterojunction solar cell using SCAPS simulation, Sol. Energy 211 (2020) 375–382, https://doi.org/10.1016/j.solener.2020.09.068.

[4] M.S. Salem, A. Shaker, M.S. Othman, A.H. Al-Bagawia, M. Fedawy, G.M. Aleid, Numerical analysis and design of high performance HTL-free antimony sulfide solar cells by SCAPS-1D, Opt. Mater. 123 (2022), https://doi.org/10.1016/j.optmat.2021.111880.

[5] J. Sun, J. Wu, X. Tong, F. Lin, Y. Wang, Z.M. Wang, Organic/Inorganic metal halide perovskite optoelectronic devices beyond solar cells, Adv. Sci. 5 (2018), 1700780, https://doi.org/10.1002/advs.201700780.

[6] E.L. Warren, M.G. Deceglie, M. Rienäcker, R. Peibst, A.C. Tamboli, P. Stradins, Maximizing tandem solar cell power extraction using a three-terminal design, Sustain. Energy Fuels 2 (2018) 1141–1147, https://doi.org/10.1039/c8se00133b.

[7] T. Todorov, O. Gunawan, S. Guha, A road towards 25% efficiency and beyond: perovskite tandem solar cells, Mol. Syst. Des. Eng. 1 (2016) 370–376, https://doi.org/10.1039/c6me00041j.

[8] I. Tobías, A. Luque, Ideal efficiency of monolithic, series-connected multijunction solar cells, Prog. Photovoltaics Res. Appl. 10 (2002) 323–329, https://doi.org/10.1002/pip.427.

[9] J. Kim, Z. Hong, G. Li, T. Bin Song, J. Chey, Y.S. Lee, J. You, C.C. Chen, D. K. Sadana, Y. Yang, 10.5% efficient polymer and amorphous silicon hybrid tandem photovoltaic cell, Nat. Commun. 6 (2015), https://doi.org/10.1038/ncomms7391.

[10] B. Liu, L. Bai, T. Li, C. Wei, B. Li, Q. Huang, D. Zhang, G. Wang, Y. Zhao, X. Zhang, High efficiency and high open-circuit voltage quadruple-junction silicon thin film solar cells for future electronic applications, Energy Environ. Sci. 10 (2017) 1134–1141, https://doi.org/10.1039/c7ee00332c.

[11] D.L. Staebler, C.R. Wronski, Reversible conductivity changes in discharge-produced amorphous Si, Appl. Phys. Lett. 31 (1977) 292–294.

[12] H. Plagwitz, B. Terheiden, R. Brendel, Staebler-Wronski-like formation of defects at the amorphous-silicon- crystalline silicon interface during illumination, J. Appl. Phys. 103 (2008), https://doi.org/10.1063/1.2913320.

[13] M.A. Green, Y. Hishikawa, E.D. Dunlop, D.H. Levi, J. Hohl-Ebinger, A.W.Y. Ho-Baillie, Solar cell efficiency tables (version 52), Prog. Photovoltaics Res. Appl. 26 (2018) 427–436, https://doi.org/10.1002/pip.3040.

[14] K. Sasaki, T. Agui, K. Nakaido, N. Takahashi, R. Onitsuka, T. Takamoto, Development of InGaP/GaAs/InGaAs inverted triple junction concentrator solar cells, in: AIP Conf. Proc., American Institute of PhysicsAIP, 2013, pp. 22–25, https://doi.org/10.1063/1.4822190.

[15] H. Cotal, C. Fetzer, J. Boisvert, G. Kinsey, R. King, P. Hebert, H. Yoon, N. Karam, III-V multijunction solar cells for concentrating photovoltaics, Energy Environ. Sci. 2 (2009) 174–192, https://doi.org/10.1039/b809257e.

[16] H. Yoon, J.E. Granata, P. Hebert, R.R. King, C.M. Fetzer, P.C. Colter, K. M. Edmondson, D. Law, G.S. Kinsey, D.D. Krut, J.H. Ermer, M.S. Gillanders, N. H. Karam, Recent advances in high-efficiency III-V multi-junction solar cells for space applications: ultra triple junction qualification, in: Prog. Photovoltaics Res. Appl., John Wiley & Sons, Ltd, 2005, pp. 133–139, https://doi.org/10.1002/pip.610.

[17] J.J. Schermer, G.J. Bauhuis, P. Mulder, W.J. Meulemeesters, E. Haverkamp, M.M. A.J. Voncken, P.K. Larsen, High rate epitaxial lift-off of inGaP films from GaAs substrates, Appl. Phys. Lett. 76 (2000) 2131–2133, https://doi.org/10.1063/1.126276.

[18] W. Choi, C.Z. Kim, C.S. Kim, W. Heo, T. Joo, S.Y. Ryu, H. Kim, H. Kim, H.K. Kang, S. Jo, A repeatable epitaxial lift-off process from a single GaAs substrate for low-cost and high-efficiency III-V solar cells, Adv. Energy Mater. 4 (2014), https://doi.org/10.1002/aenm.201400589.

[19] C. Wu, Q. Zhang, G. Liu, Z. Zhang, D. Wang, B. Qu, Z. Chen, L. Xiao, From Pb to Bi: a promising family of Pb-free optoelectronic materials and devices, Adv. Energy Mater. 10 (2020), https://doi.org/10.1002/aenm.201902496.

[20] M.S. Salem, A. Shaker, T.S. Almurayziq, M.T. Alshammari, Prospective efficiency boosting of full-inorganic single-junction Sb2(S, Se)3 solar cell, Sol. Energy Mater. Sol. Cells. 248 (2022) 112001.

[21] Y.C. Choi, D.U. Lee, J.H. Noh, E.K. Kim, S. Il Seok, Highly improved Sb_2S_3 sensitized-inorganic-organic heterojunction solar cells and quantification of traps by deep-level transient spectroscopy, Adv. Funct. Mater. 24 (2014) 3587–3592, https://doi.org/10.1002/adfm.201304238.

[22] D.H. Kim, S.J. Lee, M.S. Park, J.K. Kang, J.H. Heo, S.H. Im, S.J. Sung, Highly reproducible planar Sb_2S_3-sensitized solar cells based on atomic layer deposition, Nanoscale 6 (2014) 14549–14554, https://doi.org/10.1039/c4nr04148h.

[23] M.A. Green, Silicon wafer-based tandem cells: the ultimate photovoltaic solution?, in: Physics, Simulation, Photonic Eng. Photovolt. Devices III SPIE, 2014, p. 89810L, https://doi.org/10.1117/12.2044175.

[24] R. Kondrotas, C. Chen, J. Tang, Sb_2S_3 solar cells, Joule 2 (2018) 857–878, https://doi.org/10.1016/j.joule.2018.04.003.

[25] S. Lu, C. Chen, J. Tang, Possible top cells for next-generation Si-based tandem solar cells, Front. Optoelectron. 13 (2020) 246–255, https://doi.org/10.1007/s12200-020-1050-y.

[26] C. Gao, M. Xu, B.K. Ng, L. Kang, L. Jiang, Y. Lai, F. Liu, In situ growth of Sb_2S_3 thin films by reactive sputtering on n-Si(100) substrates for top sub-cell of silicon based tandem solar cells, Mater. Lett. 195 (2017) 186–189, https://doi.org/10.1016/j.matlet.2017.02.046.

[27] J. Zhang, W. Lian, Y. Yin, X. Wang, R. Tang, C. Qian, X. Hao, C. Zhu, T. Chen, All antimony chalcogenide tandem solar cell, Sol. RRL. 4 (2020) 1–6, https://doi.org/10.1002/solr.202000048.

[28] F. Meillaud, A. Shah, C. Droz, E. Vallat-Sauvain, C. Miazza, Efficiency limits for single-junction and tandem solar cells, Sol. Energy Mater. Sol. Cells 90 (2006) 2952–2959, https://doi.org/10.1016/j.solmat.2006.06.002.

[29] M.A. Green, E.D. Dunlop, G. Siefer, M. Yoshita, N. Kopidakis, K. Bothe, X. Hao, Solar cell efficiency tables (Version 61), Prog. Photovoltaics Res. Appl. 31 (2023) 3–16, https://doi.org/10.1002/PIP.3646.

[30] M. Okil, M.S. Salem, T.M. Abdolkader, A. Shaker, From crystalline to low-cost silicon-based solar cells : a review, Silicon (2021) 1–17, https://doi.org/10.1007/s12633-021-01032-4.

[31] S. Schafer, R. Brendel, Accurate calculation of the absorptance enhances efficiency limit of crystalline silicon solar cells with lambertian light trapping, IEEE J. Photovoltaics 8 (2018) 1156–1158, https://doi.org/10.1109/JPHOTOV.2018.2824024.

[32] I. Hwang, H.D. Um, B.S. Kim, M. Wober, K. Seo, Flexible crystalline silicon radial junction photovoltaics with vertically aligned tapered microwires, Energy Environ. Sci. 11 (2018) 641–647, https://doi.org/10.1039/c7ee03340k.

[33] W. Hadibrata, F. Es, S. Yerci, R. Turan, Ultrathin Si solar cell with nanostructured light trapping by metal assisted etching, Sol. Energy Mater. Sol. Cells 180 (2018) 247–252, https://doi.org/10.1016/j.solmat.2017.06.029.

[34] S. Wang, B.D. Weil, Y. Li, K.X. Wang, E. Garnett, S. Fan, Y. Cui, Large-area free-standing ultrathin single-crystal silicon as processable materials, Nano Lett. 13 (2013) 4393–4398, https://doi.org/10.1021/nl402230v.

[35] S. Zhou, Z. Yang, P. Gao, X. Li, X. Yang, D. Wang, J. He, Z. Ying, J. Ye, Wafer-scale integration of inverted nanopyramid arrays for advanced light trapping in crystalline silicon thin film solar cells, Nanoscale Res. Lett. 11 (2016), https://doi.org/10.1186/s11671-016-1397-6.

[36] K.J. Yu, L. Gao, J.S. Park, Y.R. Lee, C.J. Corcoran, R.G. Nuzzo, D. Chanda, J. A. Rogers, Light trapping in ultrathin monocrystalline silicon solar cells, Adv. Energy Mater. 3 (2013) 1401–1406, https://doi.org/10.1002/aenm.201300542.

[37] M. Pagliaro, R. Ciriminna, G. Palmisano, Flexible solar cells, ChemSusChem 1 (2008) 880–891, https://doi.org/10.1002/cssc.200800127.

[38] M.S. Salem, A. Zekry, A. Shaker, M. Abouelatta, T.M. Abdolkader, Performance enhancement of a proposed solar cell microstructure based on heavily doped silicon wafers, Semicond. Sci. Technol. 34 (2019), https://doi.org/10.1088/1361-6641/ab0078.

[39] M.S. Salem, A.J. Alzahrani, R.A. Ramadan, A. Alanazi, A. Shaker, M. Abouelatta, C. Gontrand, M. Elbanna, A. Zekry, Physically based analytical model of heavily doped silicon wafers based proposed solar cell microstructure, IEEE Access 8 (2020) 138898–138906, https://doi.org/10.1109/ACCESS.2020.3012657.

[40] M.M. Salah, A. Zekry, M. Abouelatta, A. Shaker, M. Mousa, F.Z. Amer, R. I. Mubarak, A. Saeed, High-efficiency electron transport layer-free perovskite/GeTe tandem solar cell: numerical simulation, Crystals 12 (2022) 878, https://doi.org/10.3390/cryst12070878.

[41] Y.Z. Hamri, Y. Bourezig, M. Medles, M. Ameri, K. Toumi, Y. Al-Douri, C.H. Voon, I. Ameri, Improved efficiency of Cu(In,Ga)Se2 thinfilm solar cells using a buffer layer alternative to CdS, Sol. Energy 178 (2019) 150–156, https://doi.org/10.1016/j.solener.2018.12.023.

[42] S. Zandi, P. Saxena, N.E. Gorji, Numerical simulation of heat distribution in RGO-contacted perovskite solar cells using COMSOL, Sol. Energy 197 (2020) 105–110, https://doi.org/10.1016/j.solener.2019.12.050.

[43] A. Bag, R. Radhakrishnan, R. Nekovei, R. Jeyakumar, Effect of absorber layer, hole transport layer thicknesses, and its doping density on the performance of perovskite solar cells by device simulation, Sol. Energy 196 (2020) 177–182, https://doi.org/10.1016/j.solener.2019.12.014.

[44] S. Michael, A.D. Bates, M.S. Green, Silvaco atlas as a solar cell modeling tool, Conf. Rec. IEEE Photovolt. Spec. Conf. (2005) 719–721, https://doi.org/10.1109/pvsc.2005.1488232.

[45] D.U. Lee, S. Woo Pak, S. Gook Cho, E. Kyu Kim, S. Il Seok, Defect states in hybrid solar cells consisting of Sb_2S_3 quantum dots and TiO_2 nanoparticles, Appl. Phys. Lett. 103 (2013), 023901, https://doi.org/10.1063/1.4813272.

[46] P. Myagmarsereejid, M. Ingram, M. Batmunkh, Y.L. Zhong, Doping strategies in Sb_2S_3 thin films for solar cells, Small 17 (2021), 2100241, https://doi.org/10.1002/smll.202100241.

[47] H. Yu, S. Ji, X. Luo, Q. Xie, Technology cad (TCAD) simulations of Mg_2Si/Si heterojunction photodetector based on the thickness effect, Sensors 21 (2021), https://doi.org/10.3390/s21165559.

[48] H. Yu, C. Gao, J. Zou, W. Yang, Q. Xie, Simulation study on the effect of doping concentrations on the photodetection properties of Mg_2Si/Si heterojunction photodetector, Photonics 8 (2021), https://doi.org/10.3390/photonics8110509.

[49] Atlas User's Manual, Silvaco Inc., Santa Clara, USA, (n.d.). https://silvaco.com/products/tcad/device_simulation/atlas/atlas.html (accessed June 1, 2022).

[50] X. Chen, Z. Jia, Z. Chen, T. Jiang, L. Bai, F. Tao, J. Chen, X. Chen, T. Liu, X. Xu, C. Yang, W. Shen, W.E.I. Sha, H. Zhu, Y.(Michael, Yang, Efficient and reproducible monolithic perovskite/organic tandem solar cells with low-loss interconnecting layers, Joule 4 (2020) 1594–1606, https://doi.org/10.1016/j.joule.2020.06.006.

[51] K.O. Brinkmann, T. Becker, F. Zimmermann, C. Kreusel, T. Gahlmann, M. Theisen, T. Haeger, S. Olthof, C. Tückmantel, M. Günster, T. Maschwitz, F. Göbelsmann, C. Koch, D. Hertel, P. Caprioglio, F. Peña-Camargo, L. Perdigón-Toro, A. Al-Ashouri, L. Merten, A. Hinderhofer, L. Gomell, S. Zhang, F. Schreiber, S. Albrecht, K. Meerholz, D. Neher, M. Stolterfoht, T. Riedl, Perovskite–organic tandem solar cells with indium oxide interconnect, Nature 604 (2022) 280–286, https://doi.org/10.1038/s41586-022-04455-0.

[52] M. Elbar, S. Tobbeche, A. Merazga, Effect of top-cell CGS thickness on the performance of CGS/CIGS tandem solar cell, Sol. Energy 122 (2015) 104–112, https://doi.org/10.1016/j.solener.2015.08.029.

[53] X. Wang, J. Li, W. Liu, S. Yang, C. Zhu, T. Chen, A fast chemical approach towards Sb_2S_3 film with a large grain size for high-performance planar heterojunction solar cells, Nanoscale 9 (2017) 3386–3390, https://doi.org/10.1039/c7nr00154a.

[54] M.S. Salem, A. Shaker, A. Zekry, M. Abouelatta, A. Alanazi, M.T. Alshammari, C. Gontand, Analysis of hybrid hetero-homo junction lead-free perovskite solar cells by scaps simulator, Energies 14 (2021) 5741, https://doi.org/10.3390/en14185741.

[55] N. Gamal, S.H. Sedky, A. Shaker, M. Fedawy, Design of lead-free perovskite solar cell using $Zn_{1-x}Mg_xO$ as ETL: SCAPS device simulation, Optik 242 (2021), 167306, https://doi.org/10.1016/j.ijleo.2021.167306.

[56] S. Yuan, H. Deng, D. Dong, X. Yang, K. Qiao, C. Hu, H. Song, H. Song, Z. He, J. Tang, Efficient planar antimony sulfide thin film photovoltaics with large grain and preferential growth, Sol. Energy Mater. Sol. Cells 157 (2016) 887–893, https://doi.org/10.1016/j.solmat.2016.07.050.

[57] H. Chen, Z.Q. Li, B. Sun, X.D. Feng, Towards high-efficiency planar heterojunction antimony sulfide solar cells, Opt. Mater. 121 (2021), 111556, https://doi.org/10.1016/j.optmat.2021.111556.

[58] M.S. Salem, A. Shaker, M.S. Othman, A.H. Al-Bagawia, M. Fedawy, G.M. Aleid, Numerical analysis and design of high performance HTL-free antimony sulfide solar cells by SCAPS-1D, Opt. Mater. 123 (2022), 111880, https://doi.org/10.1016/j.optmat.2021.111880.

[59] X. Wang, J. Li, W. Liu, S. Yang, C. Zhu, T. Chen, A fast chemical approach towards Sb_2S_3 film with a large grain size for high-performance planar heterojunction solar cells, Nanoscale 9 (2017) 3386–3390, https://doi.org/10.1039/c7nr00154a.

[60] I. Hwang, Y. Jeong, Y. Shiratori, J. Park, S. Miyajima, I. Yoon, K. Seo, Effective photon management of non-surface-textured flexible thin crystalline silicon solar cells, Cell Reports Phys. Sci. 1 (2020), 100242, https://doi.org/10.1016/j.xcrp.2020.100242.

[61] T. Deng, Z. Xu, Y. Yamashita, T. Sato, K. Toko, T. Suemasu, Modeling the effects of defect parameters on the performance of a p-$BaSi_2$/n-Si heterojunction solar cell, Sol. Energy Mater. Sol. Cells 205 (2020), https://doi.org/10.1016/j.solmat.2019.110244.

[62] J.P. Mailoa, C.D. Bailie, E.C. Johlin, E.T. Hoke, A.J. Akey, W.H. Nguyen, M. D. McGehee, T. Buonassisi, A 2-terminal perovskite/silicon multijunction solar cell enabled by a silicon tunnel junction, Appl. Phys. Lett. 106 (2015), 121105, https://doi.org/10.1063/1.4914179.

[63] Y. Yuan, J. Huang, G. Li, Intermediate layers in tandem organic solar cells, Greenpeace 1 (2011) 65–80, https://doi.org/10.1515/green.2011.009.

[64] K.A. Bush, A.F. Palmstrom, Z.J. Yu, M. Boccard, R. Cheacharoen, J.P. Mailoa, D. P. McMeekin, R.L.Z. Hoye, C.D. Bailie, T. Leijtens, I.M. Peters, M.C. Minichetti, N. Rolston, R. Prasanna, S. Sofia, D. Harwood, W. Ma, F. Moghadam, H.J. Snaith, T. Buonassisi, Z.C. Holman, S.F. Bent, M.D. McGehee, 23.6%-efficient monolithic perovskite/silicon tandem solar cells with improved stability, Nat. Energy 2 (2017) 1–7, https://doi.org/10.1038/nenergy.2017.9.

[65] L.L. Yan, C. Han, B. Shi, Y. Zhao, X.D. Zhang, A review on the crystalline silicon bottom cell for monolithic perovskite/silicon tandem solar cells, Mater. Today Nano. 7 (2019), https://doi.org/10.1016/j.mtnano.2019.100045.

[66] Y. Wu, D. Yan, J. Peng, T. Duong, Y. Wan, S.P. Phang, H. Shen, N. Wu, C. Barugkin, X. Fu, S. Surve, D. Grant, D. Walter, T.P. White, K.R. Catchpole, K.J. Weber, Monolithic perovskite/silicon-homojunction tandem solar cell with over 22% efficiency, Energy Environ. Sci. 10 (2017) 2472–2479, https://doi.org/10.1039/c7ee02288c.

[67] C. Chen, J. Tang, Open-circuit voltage loss of antimony chalcogenide solar cells: status, origin, and possible solutions, ACS Energy Lett. 5 (2020) 2294–2304, https://doi.org/10.1021/acsenergylett.0c00940.

[68] C.E. Patrick, F. Giustino, Structural and electronic properties of semiconductor-sensitized solar-cell interfaces, Adv. Funct. Mater. 21 (2011) 4663–4667, https://doi.org/10.1002/adfm.201101103.

[69] P. Qin, S. Tanaka, S. Ito, N. Tetreault, K. Manabe, H. Nishino, M.K. Nazeeruddin, M. Grätzel, Inorganic hole conductor-based lead halide perovskite solar cells with 12.4% conversion efficiency, Nat. Commun. 5 (2014), https://doi.org/10.1038/ncomms4834.

[70] J. Xiang, Y. Li, F. Huang, D. Zhong, Effect of interfacial recombination, bulk recombination and carrier mobility on the: J - V hysteresis behaviors of perovskite solar cells: a drift-diffusion simulation study, Phys. Chem. Chem. Phys. 21 (2019) 17836–17845, https://doi.org/10.1039/c9cp03548f.

[71] T. Minemoto, M. Murata, Theoretical analysis on effect of band offsets in perovskite solar cells, Sol. Energy Mater. Sol. Cells 133 (2015) 8–14, https://doi.org/10.1016/j.solmat.2014.10.036.

[72] R. Scheer, H.W. Schock, Chalcogenide Photovoltaics: Physics, Technologies, and Thin Film Devices, John Wiley & Sons, 2011, https://doi.org/10.1002/9783527633708.

[73] C. Chen, X. Liu, K. Li, S. Lu, S. Wang, S. Li, Y. Lu, J. He, J. Zheng, X. Lin, J. Tang, High-efficient Sb_2Se_3 solar cell using $Zn_xCd_{1-x}S$ n-type layer, Appl. Phys. Lett. 118 (2021), 172103, https://doi.org/10.1063/5.0030430.

[74] Y. Zhou, Y. Li, J. Luo, D. Li, X. Liu, C. Chen, H. Song, J. Ma, D.J. Xue, B. Yang, J. Tang, Buried homojunction in CdS/Sb_2Se_3 thin film photovoltaics generated by interfacial diffusion, Appl. Phys. Lett. 111 (2017), 013901, https://doi.org/10.1063/1.4991539.

[75] Z.H. Li, E.S. Cho, S.J. Kwon, Mg-doped ZnO thin films deposited by the atomic layer chemical vapor deposition for the buffer layer of CIGS solar cell, Appl. Surf. Sci. 314 (2014) 97–103, https://doi.org/10.1016/j.apsusc.2014.06.136.

[76] L.Y. Lin, Y. Qiu, Y. Zhang, H. Zhang, Analysis of effect of Zn(O,S) buffer layer properties on CZTS solar cell performance using AMPS, Chin. Phys. Lett. 33 (2016), https://doi.org/10.1088/0256-307X/33/10/107801.

[77] I. Gharibshahian, A.A. Orouji, S. Sharbati, Efficient $Sb_2(S,Se)_3$/Zn(O,S) solar cells with high open-circuit voltage by controlling sulfur content in the absorber-buffer layers, Sol. Energy 227 (2021) 606–615, https://doi.org/10.1016/j.solener.2021.09.039.

[78] K. Tanaka, T. Minemoto, H. Takakura, Analysis of heterointerface recombination by Zn1-xMgxO for window layer of Cu(In,Ga)Se2 solar cells, Sol. Energy 83 (2009) 477–479, https://doi.org/10.1016/j.solener.2008.09.003.

[79] R. Kondrotas, C. Chen, J. Tang, Sb_2S_3 solar cells, Joule 2 (2018) 857–878, https://doi.org/10.1016/j.joule.2018.04.003.

[80] A. Zekry, A. Shaker, M. Salem, Solar cells and arrays: principles, analysis, and design, in: Adv. Renew. Energies Power Technol., Elsevier, 2018, pp. 3–56, https://doi.org/10.1016/B978-0-12-812959-3.00001-0.

[81] M.A. Green, Accurate expressions for solar cell fill factors including series and shunt resistances, Appl. Phys. Lett. 108 (2016), 081111, https://doi.org/10.1063/1.4942660.

[82] U. Wurfel, A. Cuevas, P. Wurfel, Charge carrier separation in solar cells, IEEE J. Photovoltaics 5 (2015) 461–469, https://doi.org/10.1109/JPHOTOV.2014.2363550.

[83] H. Deng, Y. Zeng, M. Ishaq, S. Yuan, H. Zhang, X. Yang, M. Hou, U. Farooq, J. Huang, K. Sun, R. Webster, H. Wu, Z. Chen, F. Yi, H. Song, X. Hao, J. Tang, Quasiepitaxy strategy for efficient full-inorganic Sb_2S_3 solar cells, Adv. Funct. Mater. 29 (2019), https://doi.org/10.1002/adfm.201901720.

[84] L. Zhang, W. Lian, X. Zhao, Y. Yin, T. Chen, C. Zhu, Sb_2S_3 Seed-Mediated growth of low-defect Sb_2S_3 on a TiO_2 Substrate for efficient solar cells, ACS Appl. Energy Mater. 3 (2020) 12417–12422, https://doi.org/10.1021/acsaem.0c02400.

[85] J. Dong, Y. Liu, Z. Wang, Y. Zhang, Boosting V_{OC} of antimony chalcogenide solar cells: a review on interfaces and defects, Nano Sel 2 (2021) 1818–1848, https://doi.org/10.1002/nano.202000288.

[86] A. Basak, U.P. Singh, Numerical modelling and analysis of earth abundant Sb_2S_3 and Sb_2Se_3 based solar cells using SCAPS-1D, Sol. Energy Mater. Sol. Cells 230 (2021), 111184, https://doi.org/10.1016/j.solmat.2021.111184.

[87] Y. Xiao, H. Wang, H. Kuang, Numerical simulation and performance optimization of Sb_2S_3 solar cell with a hole transport layer, Opt. Mater. 108 (2020), 110414, https://doi.org/10.1016/j.optmat.2020.110414.

[88] F. Ayala-Mató, O. Vigil-Galán, M.M. Nicolás-Marín, M. Courel, Study of loss mechanisms on $Sb_2(S_{1-x}Se_x)_3$ solar cell with n-i-p structure: toward an efficiency promotion, Appl. Phys. Lett. 118 (2021), https://doi.org/10.1063/5.0032867.

[89] Y. Zhao, C. Li, J. Niu, Z. Zhi, G. Chen, J. Gong, J. Li, X. Xiao, Zinc-based electron transport materials for over 9.6%-efficient S-rich $Sb_2(S,Se)_3$ solar cells, J. Mater. Chem. A. 9 (2021) 12644–12651, https://doi.org/10.1039/d1ta02356j.

[90] Best research-cell efficiency chart provided by NREL (n.d.), https://www.nrel.gov/pv/assets/pdfs/best-research-cell-efficiencies.pdf. (Accessed 22 January 2023).

[91] D. Yang, X. Zhang, Y. Hou, K. Wang, T. Ye, J. Yoon, C. Wu, M. Sanghadasa, S. Frank, S. Priya, 28.3%-efficiency perovskite/silicon tandem solar cell by optimal transparent electrode for high efficient semitransparent top cell, Nano Energy 84 (2021), https://doi.org/10.1016/j.nanoen.2021.105934, 105934-1-105934–9.

[92] K. Amri, R. Belghouthi, M. Aillerie, R. Gharbi, Device optimization of a lead-free perovskite/silicon tandem solar cell with 24.4% power conversion efficiency, Energies 14 (2021), https://doi.org/10.3390/en14123383.

[93] M. Bacha, A. Saadoune, I. Youcef, O. terghini, Design and numerical investigation of Perovskite/Silicon tandem solar cell, Opt. Mater. 131 (2022), 112671, https://doi.org/10.1016/j.optmat.2022.112671.

[94] M. Mousa, M.M. Salah, F.Z. Amer, A. Saeed, R.I. Mubarak, High efficiency tandem perovskite/CIGS solar cell, in: 2020 2nd Int. Conf. Smart Power Internet Energy Syst, SPIES 2020, 2020, pp. 224–227, https://doi.org/10.1109/SPIES48661.2020.9242927.